Journal of Applied Physics

Three-dimensional visualization of Sb segregation in InAs/InAsSb superlattices using atom probe tomography

Cite as: J. Appl. Phys. **128**, 015302 (2020); https://doi.org/10.1063/1.5143446
Submitted: 23 December 2019 . Accepted: 01 June 2020 . Published Online: 01 July 2020

Nicole A. Kotulak, Jill A. Nolde, Michael B. Katz, Mark E. Twigg, Keith E. Knipling, Dmitri Lubyshev, Joel M. Fastenau, Amy W. K. Liu, and Edward H. Aifer

ARTICLES YOU MAY BE INTERESTED IN

Vertical carrier transport in strain-balanced InAs/InAsSb type-II superlattice material
Applied Physics Letters **116**, 182109 (2020); https://doi.org/10.1063/1.5144079

Study of vertical hole transport in InAs/InAsSb type-II superlattices by steady-state and time-resolved photoluminescence spectroscopy
Applied Physics Letters **116**, 201108 (2020); https://doi.org/10.1063/1.5144888

Dual crystallization modes of sputter-deposited amorphous SiGe films
Journal of Applied Physics **128**, 015303 (2020); https://doi.org/10.1063/5.0010202

Lock-in Amplifiers up to 600 MHz

Three-dimensional visualization of Sb segregation in InAs/InAsSb superlattices using atom probe tomography

Cite as: J. Appl. Phys. **128**, 015302 (2020); doi: 10.1063/1.5143446
Submitted: 23 December 2019 · Accepted: 1 June 2020 ·
Published Online: 1 July 2020

View Online

Export Citation

CrossMark

Nicole A. Kotulak,[1] Jill A. Nolde,[1,a)] Michael B. Katz,[1] Mark E. Twigg,[1] Keith E. Knipling,[1] Dmitri Lubyshev,[2] Joel M. Fastenau,[2] Amy W. K. Liu,[2] and Edward H. Aifer[1]

AFFILIATIONS

[1]U.S. Naval Research Laboratory, Washington, DC 20375, USA
[2]IQE Inc., Bethlehem, Pennsylvania 18015, USA

[a)]**Author to whom correspondence should be addressed:** jill.nolde@nrl.navy.mil

ABSTRACT

The Sb concentration profile in an *nBn* photodetector containing an InAs/InAsSb type-II superlattice is collected and analyzed using atom probe tomography. A 3D reconstruction comprises the full composition of 31 periods. The Sb concentration profile is evaluated for the entire 31 period stack, as well as each individual period using segregation models from Muraki and Wood. Trends in the asymmetric Sb profile show a consistent non-negligible Sb concentration in the InAs layers and a lower Sb concentration in the InAsSb with respect to the target concentration.

https://doi.org/10.1063/1.5143446

I. INTRODUCTION

The current research paths for midwave infrared (MWIR) photodetectors are dominated by the need for higher temperature operation, enabling MWIR imaging for a broader range of applications with strict requirements for size, weight, and power. Very recently, InAs/InAsSb type-II superlattices (T2SLs) have come to the forefront of this area due to minority carrier lifetimes 10–100 times longer than earlier InAs/Ga(In)Sb T2SLs.[1] Combined with heterojunction designs such as the *nBn*, devices using these SLs have demonstrated exceptional performance at higher operating temperatures than incumbent III–V-based InSb photodetectors.[2] However, design of these SLs is non-trivial due to the complex growth kinetics of incorporating large Sb adatoms into a matrix of smaller atoms. This issue has been observed within InAs/InAsSb SL development,[3–5] as well as other Sb-containing device structures,[6–8] in which Sb does not remain strictly within the intended layer and does not incorporate at the concentrations expected based on the flux of atoms to the growth interface.

The segregation of non-common atoms at a growth interface and into the following layer leads to non-abrupt and asymmetric interfaces, which can cause changes to the optoelectronic properties of the T2SL, including fundamental parameters such as bandgap, valence/conduction band offsets, and carrier mobility.[7,9,10] For T2SL devices, that rely on the precise engineering of these optoelectronic properties in order to attain the desired cutoff wavelength, avoid excess applied bias requirements, or have the necessary carrier diffusion length for high quantum efficiency, non-abrupt interfaces can limit the performance impacting suitability for specific tasks and environments[11] or make the design and growth of such structures a time-consuming trial-and-error process. With further understanding of the SL composition within the growth plane and along the growth direction, the bond characteristics and Sb concentration profile can be incorporated into theoretical models enabling better, more accurate design of photodetectors for the MWIR, as well as longwave and very longwave IR.[12,13]

Previous studies have used techniques such as transmission electron microscopy (TEM) and scanning tunneling microscopy (STM) to map the location of Sb within these III–V systems in an effort to identify the nature of the interfaces and understand the growth kinetics governing Sb incorporation and segregation.[3–8] Both systems are well-suited to the analysis, with the capability of producing atomic-scale resolution for visualizing precise atom location, enabling more accurate theoretical models.

Atom probe tomography (APT) is a characterization technique that provides 3D compositional profiles down to sub-nm resolution scales. Like TEM and STM, the profile of Sb throughout the films, and across the interfaces, can be determined. In addition, there is the capability of visualizing the interfaces in three dimensions, which can elucidate any nonuniformity in the growth plane. The technique has been used in the past to evaluate compound semiconductors with indications that near atomic spatial resolution can be achieved.[14–17] For this work, APT is used to collect chemical species identity and location data for a Ga-free MWIR SL structure to evaluate the level of integration of Sb in the material, as well as location profile across the periods that could affect interface characteristics.

II. EXPERIMENTAL METHODS

The material investigated here is a MWIR *nBn* T2SL photodetector consisting of 734 periods ($\approx 4\,\mu$m thick) of a 42.6 Å InAs/11.9 Å InAsSb SL with a targeted Sb concentration of 46.7%, followed by an electron barrier of 150 nm AlGaAsSb and a ≈300-nm-thick contact layer composed of an InAs/InAsSb SL.[18,19] The T2SL photodetector structure was grown in an Oxford-VG V-100 molecular beam epitaxy (MBE) tool using a production epitaxial growth process for Sb-based materials developed at IQE.[20–22] The As and Sb group V elements were provided by valved cracker sources, while the In, Ga, and Al group III molecular beams were produced in SUMO® or conical effusion cells. The detectors were grown on 100 mm diameter, low (Te $\leq 2 \times 10^{17}\,\text{cm}^{-3}$) *n*-doped (001) GaSb substrates at growth temperatures ranging from 400 to 520 °C depending on the specific alloys. The AlGaAsSb layer is mostly AlSb with the addition of Ga to improve the valence band alignment and As to lattice-match the layer. During the growth of the absorber layer for this particular sample, two growth interrupts at periods 704 and 714 were employed to facilitate cell temperature changes. These interrupts were programmed at the end of the InAsSb layer within the SL sequence and lasted several minutes with an As overpressure. From analysis and fitting of the (004) high-resolution XRD (HRXRD) spectrum, the SL period is 58.27 Å and the Sb composition in the hole well is 46.4%. Photodetectors fabricated from this wafer displayed typical device performance expected for the given design, which was similar to the results presented in Refs. 2, 18, and 19.

Since we are most interested in the composition profile in the absorber layer, the SL above the barrier was removed using a highly selective $C_6H_8O_7$ and H_2O_2 mixture. The barrier layer was left in place as the sacrificial material for the APT specimen formation. Specimen preparation was performed on an FEI Nova 600 NanoLab DualBeam™ focused ion beam/scanning electron microscope (FIB/SEM) according to standard lift-out and milling procedures.[23] Specimens were mounted onto flat-topped Si microtip arrays and sharpened to an end-radius of ≈30−40 nm. An example specimen is shown in Fig. 1.

APT data were collected with a Cameca 4000X Si Local Electrode Atom Probe (LEAP). Run parameters were set to 25 K base temperature, 0.01 pJ nominal laser pulse energy, a pulse repetition rate of 125 kHz, and an 0.5% detection rate or 5 ions per 1000 pulses. Analysis and 3D reconstruction of the data were performed with the Cameca IVAS 3.8.0 software suite. A portion of the absorber SL was evaporated and analyzed.

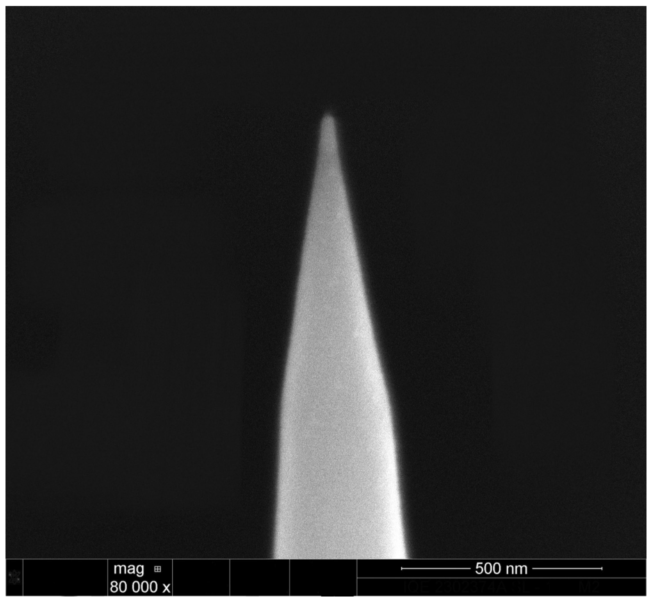

FIG. 1. APT-ready InAs/InAsSb superlattice specimen.

III. RESULTS AND DISCUSSION

A. Mass spectrum and 3D reconstruction

The mass spectrum is presented in Fig. 2, with peak labeling as shown. The fidelity of the spectrum, with sharp peaks and minimal multi-element species, suggests high data quality for reconstruction and analysis purposes. Fitting the spectrum followed

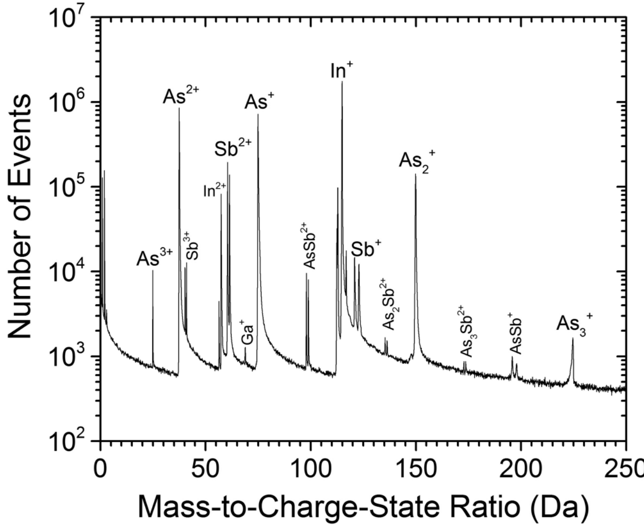

FIG. 2. Time-of-flight mass spectrum of the sample, with the analysis region containing the InAs/InAsSb SL structure.

existing conventions, as well as composition as determined through correlative characterization.[24]

The 3D reconstruction was accomplished using the half shank angle of the original specimen shape, as determined through SEM imaging after the final low-kV clean, combined with an interface flattening algorithm, both standard in the IVAS 3.8.0 software. No additional algorithms were required to improve the reconstruction, as the dimensions of the SL layers corresponded to thicknesses determined through additional characterization means. Upon reconstruction, the Sb is observed to be dispersed throughout the SL structure, rather than contained to only the designated InAsSb layers, as seen in the center reconstruction of Fig. 3(b). Additionally, an InAsSb layer showing little to no Sb content was discovered, as shown in Fig. 3. This feature was also observed in TEM, providing an additional indicator of the reliability of the reconstruction [see Fig. 3(a)]. Through TEM, the periods of the SL were individually counted such that the two regions in Fig. 3(a) with a greatly diminished Sb concentration could be directly correlated to the two growth interrupts at periods 704 and 714. These interrupts appear to have facilitated the out-diffusion of Sb and/or As–Sb exchange reactions at the exposed InAsSb surface, resulting in a greatly diminished Sb concentration in those particular periods. These unintended abnormal periods with "missing Sb" enable the exact identification of the investigated periods relative to the AlGaAsSb layer. In Fig. 3(b), one of the two missing periods (704) is visible in the reconstruction, indicating that about 128 nm of the absorber SL, in addition to the 150 nm barrier layer, was removed during the specimen preparation. A step-like edge is also visible in the reconstruction and is a known artifact of the interface flattening algorithm.

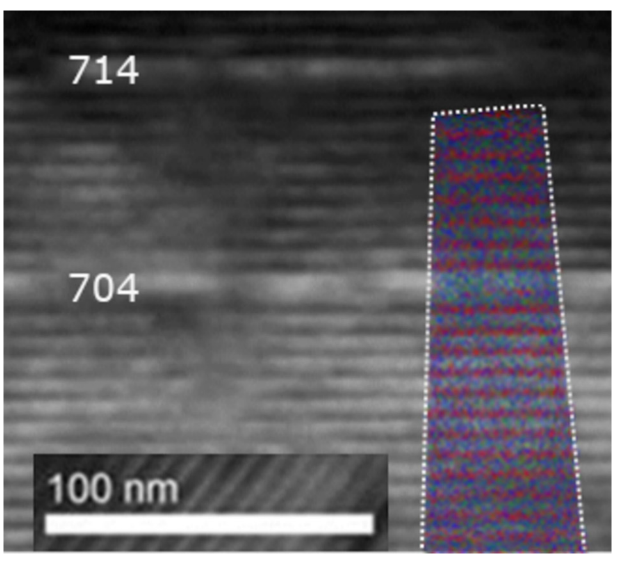

(a)

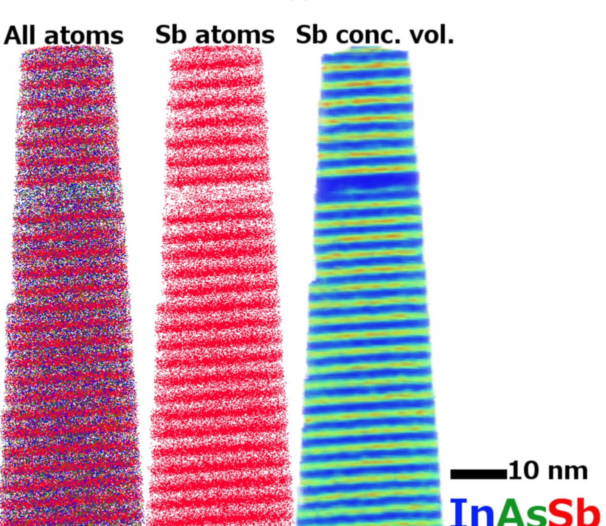

(b)

FIG. 3. (a) TEM micrograph of the SL structure with the APT reconstruction overlayed. The periods containing growth interrupts (704, 714) are labeled. Alternating InAs/InAsSb layers are visible, as well as a skipped InAsSb layer, corresponding to the structures visible by TEM. (b) Volume reconstructions of the SL structure. (Left) Full reconstruction, with each dot indicating a recorded atom; (center) reconstruction showing only the Sb atoms; and (right) Sb concentration volume, with blue indicating a low Sb concentration and red indicating a high Sb concentration.

It should be noted that, despite In being the only group III element present in the specimen, the composition of In as viewed by 1D composition profiles along the growth axis did not meet or maintain 50% total composition (100% with respect to group III only) across the specimen analysis region as would be expected. No correlative characterization results indicated a growth anomaly that would account for this discrepancy. It has been documented in the literature, however, that chemical analysis of InAs/InAsSb via TEM also exhibits the same In deficiency.[7] This documented phenomenon indicates a unique challenge in accurately accounting for In in these structures that is beyond the scope of this study.

B. Analysis of antimony concentration profile

Within the 3D reconstruction, a region of interest (ROI) $20 \times 20 \times 260\,nm^3$ was identified for further analysis of the Sb composition. Within the ROI, interfaces were set as isoconcentration surfaces at 9% Sb. These interfaces are shown in Fig. 4(a) (Multimedia view). Also shown are the locations of Sb atoms, which have a high density in alternating layers. These high density regions correspond to InAsSb layers; however, Sb is also observed within the InAs layers. This view of the SL structure displays the 3D nature of the interfaces between the InAsSb and InAs layers in which it is clear that the isoconcentration surfaces are not atomically flat. Furthermore, in the first full InAsSb layer from the bottom, the isoconcentration surfaces actually intersect on the right side. Only with a full 3D visualization can these interesting features be identified.

Initial quantitative analysis of the Sb concentration throughout the ROI was performed by a 1D composition profile of the Sb along the z-axis/growth direction of the specimen, as shown in Fig. 4(b)

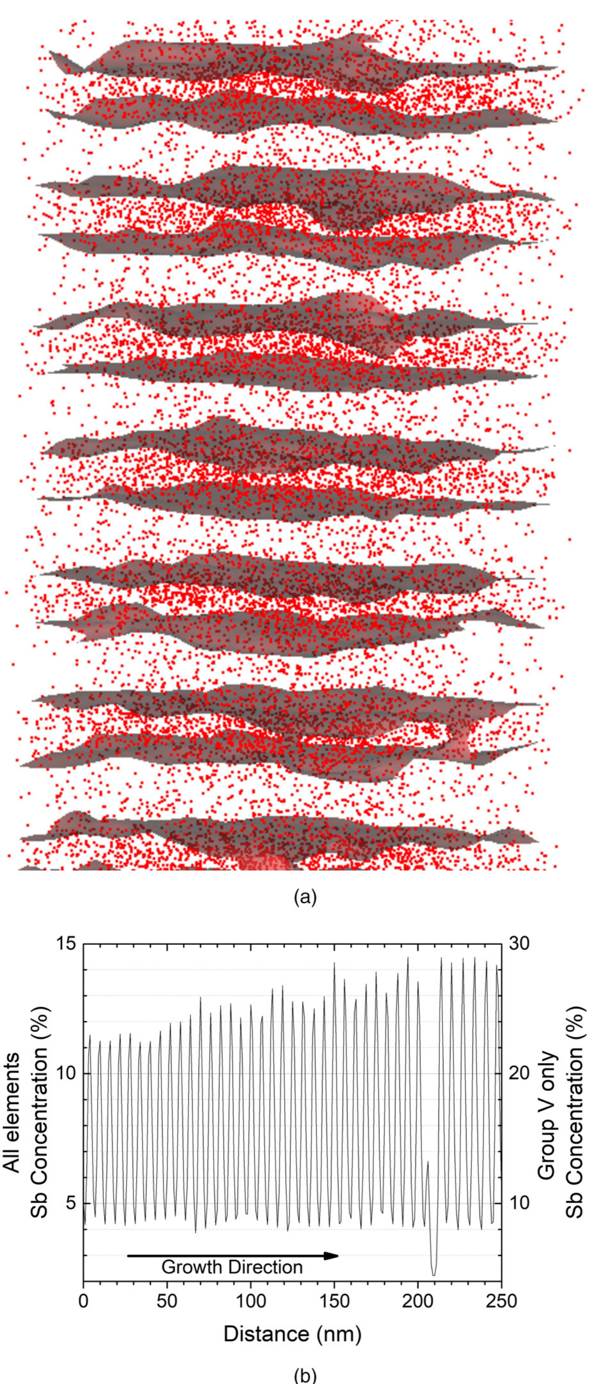

FIG. 4. (a) A portion of the ROI with isoconcentration surfaces at 9% Sb with respect to total concentration values (18% group V only) to identify interfaces between InAs and InAsSb layers. Red dots represent individual Sb atoms. (b) 1D profile of the Sb concentration along the growth direction of the SL. $x = 0$ corresponds to the SL layers closer to the substrate, and $x = 250$ corresponds to the point at which evaporation initiated (toward the surface of the structure). Multimedia view: https://doi.org/10.1063/1.5143446.1

(Multimedia view), with a z step size of 0.25 nm. Typically, reconstructions describe the composition of each element as a percentage of the total including both group III and group V constituents, as shown on the left axis. Henceforth, we will describe the Sb concentration in the more typical fashion as a percentage of group V elements, as shown on the right axis.

The first noticeable feature is the drop in the Sb concentration associated with the documented growth interrupts. In addition, the minimum Sb concentration is nominally consistent at 8%–9%, except for during the interrupt, where the minimum Sb drops to nearly 4%. This confirms the qualitative observation that Sb exists in non-trivial quantities in the InAs layers of the structure, as the minimum Sb concentration never reaches the desired 0%. This region with depleted levels of Sb is evidence of the strength of the intermixing and substitution process, which occurs between Sb and As. The peak of the Sb composition should have occurred at $x \approx 207$ nm on the plot, instead over a depth of several nm the Sb composition is reduced. If an As–Sb exchange reaction was occurring entirely on the surface, the top monolayer ($\approx$3 Å) would have reduced Sb, but the reduction has occurred several monolayers below the surface as predicted by *ab initio* calculations.[25]

Another feature of note is the evolution of the maximum Sb concentration throughout the growth. Across these periods, the maximum Sb concentration increases from $\approx$22%–23% in the layers grown closest to the substrate to $\approx$28%–29% in the later InAsSb layers. The step size used for this profile was chosen to visualize the global Sb fluctuations through the analyzed region, but only 4–5 points will fall within the InAsSb layer. As a result, the peak Sb values may be missed in some periods such that these maximum values may not be accurate.

In order to evaluate a more detailed Sb concentration profile, a 1D contour was made perpendicular to the initial InAsSb interface in each period to encompass part of the InAs layers before and after the InAsSb layer, with a z step size of 0.1 nm. The length of the profile scan is 8 nm, which fully encompasses more than an entire InAsSb/InAs period, as the period length is 5.827 nm and enables further profile analysis to fully model both the InAsSb and InAs regions. The results of the 31 analyzed periods are shown in Fig. 5. As seen in these profiles, the peak Sb concentration ranges from 33% to 45%, which is a 2%–14% deficiency from the targeted 46.7% Sb composition in the InAsSb layer. Further, as seen previously, the Sb composition does not reach 0% in the InAs film, with a minimum Sb concentration of 4%–10% Sb being present throughout the SL structure. Both divergences from the target Sb concentration observed at minimum and peak values are commonly seen in studies of mixed group V materials containing Sb.[4,5,7] As previously noted, the HRXRD data fitting suggests a 46.4% Sb concentration in this layer, which is close to the target composition. To determine this value, the model used to fit the HRXRD data assumes pure InAs and attributes all Sb to the InAsSb layers. As shown from the APT Sb composition profile, the binary analysis required for the HRXRD fit does not fully capture the nuances of the Sb profile, accounting for the discrepancy in peak concentration values between the two techniques. More complex models can be used, which separate the period into 5–8 layers with varying Sb concentrations, but unique fits require multiple diffraction spectra over a wider range of angles than is typically performed.

To further characterize the Sb concentration, the concatenated data were fit with a segregation model from Muraki *et al.*,[26] which has been used in the literature for evaluating Sb segregation in SLs with additional modifications by Wood *et al.*[3] The model has two main segments,

$$x = x_{ss}(1 - R^z) + x_0 \quad \text{for } 0 < z \le d, \qquad (1)$$
$$x = x_{ss}(1 - R^d)R^{z-d} + x_0 \quad \text{for } d < z \le P,$$

where x is the Sb composition at a location z along the growth direction, x_{ss} is the steady-state Sb composition expected if the layer was allowed to reach Sb saturation, and x_0 is the background Sb concentration expected to be present throughout the entire structure. Note that $z = 0$ does not correspond to the zero of the x axis in Fig. 5, which corresponds to the 18% Sb isoconcentration surfaces. The variable d represents the distance between the minimum and peak Sb values, corresponding to the time in which the Sb shutter would be open during growth and P is the SL period. Finally, R is the segregation probability, defining the fraction of Sb from the topmost unit layer that does not incorporate and moves to the next unit layer for possible incorporation. In Muraki's original formulation, z was in units of monolayers (MLs) since this is the most relevant unit for describing growth kinetics. However, the native units in APT are nanometers; therefore, our analysis will be primarily in these units. For this analysis, the period was fixed at the value from HRXRD $P = 5.827$ nm. Since the growth is controlled by the group III (In) flux, the ratio of the InAs and InAsSb layer thicknesses will be constant, which fixes d relative to P. The variables x_{ss}, x_0, and R were allowed to fit to the composition profile, enabling determination of the values that would best match the background and steady-state Sb concentrations over the range of layers, as well as the most representative segregation probability. The resulting fit with $x_{ss} = 49.2\%$, $x_0 = 5.7\%$, and $R = 0.423$ is shown as the red curve in Fig. 5, overlayed on the Sb concentration profiles.

There are three regions within the fit: (1) an Sb tail from the previous InAsSb layer, (2) a region of increasing Sb content that corresponds to d, and (3) a region of decreasing Sb content after the shutter has been closed. In both regions 1 and 3, the Sb concentration approaches the background Sb (x_0) value from the fit within the given InAs layer thickness. However, the InAsSb layers of region 2 are not thick enough to reach the steady-state x_{ss} value.

The segregation probability, R, in this fit is 42.3%, which indicates the amount of Sb in 1 nm of growth that does not incorporate into that nm of growth and instead moves to the next nm of growth as Sb available for incorporation—independent of the type of the layer being grown. For additional InAsSb growth, it is added to Sb adatoms present due to the Sb flux, and for InAs growth, it is a source of Sb that would not otherwise be present. In order to compare to previous studies of Sb segregation, a variable transformation of z from nm to ML is required, where $R_{ML} = R_{nm}^{a_0/2}$ and a_0 is the lattice constant. Using the lattice constant of GaSb (0.609 59 nm), $R_{ML} = 0.769$, which is within the range observed in other work (0.746–0.81).[4,5]

The background Sb concentration within the InAs layer, x_0, is similar to other evaluations of InAs/InAsSb SL structures[5,7] but is high when compared with other mixed anion Sb-containing growth systems.[27,28] Comparing the structure evaluated here with those in the literature shows that the layer thicknesses are dramatically different, which may explain the difference in background Sb. In this work, the InAs layers must be thin (≈4 nm) to facilitate optical absorption and carrier mobility for high performance but are not thick enough to allow x_0 to reach zero (i.e., Sb-free InAs) because the In–Sb bond is much weaker than the In–As bond.[29] As a result of the difference in bond strength, Sb will "float" (i.e., incorporate less) on the growth surface. Then, during the InAs layer growth, the excess Sb will slowly incorporate into the film leaving a large amount of Sb within that layer. In comparison, evaluations of GaAsSb quantum dots grown on GaAs have shown a negligible Sb concentration in the 50 nm GaAs spacer region, an order of magnitude greater thickness in which surface Sb can incorporate.[27,28] The Sb concentration in the InAsSb/InAs SL should similarly reduce as the InAs layer thickness increases, but it is likely to require at least 10 nm of total InAs growth to achieve an appreciable reduction in background Sb.[30]

Luna *et al.*[31,32] devised another commonly used model based on two dimensional growth dynamics, which results in a sigmoidal function with an interface width, L, that depends on the growth rate, material flux, and sticking coefficients. The model has two separate segments defining the lower and upper interface of a quantum well (QW),

$$x = \frac{x_{ss}^l}{1 + e^{-(z+N_w)/L_l}} + x_0 \quad \text{for } z \le 0, \qquad (2)$$
$$x = x_{ss}^u - \frac{x_{ss}^u}{1 + e^{-(z-N_w)/L_u}} + x_0 \quad \text{for } z > 0,$$

where x, z, x_0, and x_{ss} have the same meaning as in the Muraki/Wood model, N_w is the half-width of the QW, and $L_{l,u}$ is the interface width of the lower/upper interface. In this model, the lower and upper interfaces have different steady-state Sb compositions denoted $x_{ss}^{l,u}$. For analyzing this material, $2N_w$ corresponds to the thickness of the InAsSb layer and is equal to d from the Muraki model. Note that $z = 0$ is different from in the Muraki model and corresponds to the center of the QW, which again does not correspond to the zero of the x axis in Fig. 5. The variables $x_{ss}^{l,u}$, x_0, and $L_{l,u}$ were allowed to fit to the composition profile, resulting in $x_{ss}^l = 34.7\%$, $x_{ss}^u = 42.5\%$, $x_0 = 6.4\%$, $L_l = 0.325$ nm, and $L_u = 0.69$ nm as shown by the blue curve in Fig. 5.

The background Sb concentration x_0 is slightly higher than in the Muraki model but of a similar magnitude. Both of the x_{ss} values are lower than the Muraki result, implying that Sb incorporated into the InAsSb is much closer to the saturation values expected based on the Sb flux. Additionally, both x_{ss} values are less than the nominal design value for Sb as well as the value extracted from XRD. As a result, this fit parameter is questionable. Finally, to compare the segregation levels from each fit, we can calculate the segregation length[26] $\lambda = -a_0/(2 \ln R_{ML}) = 1.16$ nm, where a_0 is the lattice constant of GaSb. The segregation length from the Muraki model is significantly larger than both the interface widths from the sigmoidal fit.

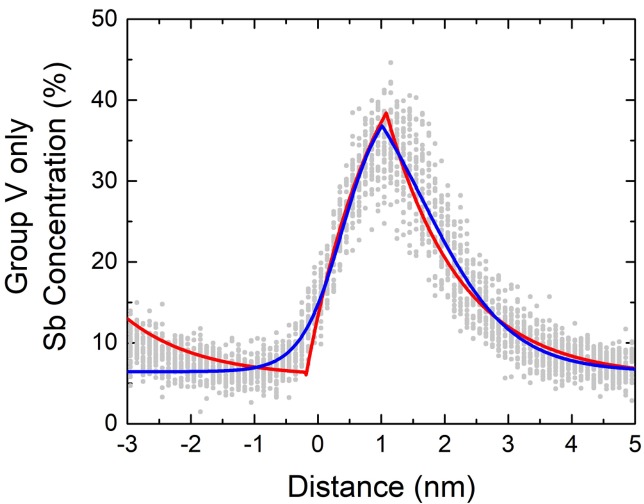

FIG. 5. 1D composition profiles of Sb across the InAsSb layer. On the x axis, $x = 0$ marks the initial InAsSb interface at 18% Sb, $x < 0$ is the InAs layer grown before, and $x > 0$ is the growth of InAsSb followed by the next InAs. The fit of the concatenated data with Muraki (red) and sigmoidal models (blue) is shown.

Previous work that used both models showed that the sigmoidal fit was more accurate for the lower interface, while the Muraki model was a better fit for the upper interface.[4] The same conclusion cannot be made about our data. The difference may be a result of the larger amount of data being fit here vs previous work in which a single period of the SL was fit. The sigmoidal relation more accurately models the minimal intrinsic interface width based on surface–adatom interactions.[4] Therefore, this model fits the initial turn-on of the Sb concentration ($-0.75 < x < 0.1$) much better than the Muraki model. However, the sigmoidal model assumes a structure in which a single QW layer is surrounded by much thicker spacer/barrier layers, in which the segregating species would be allowed to fully incorporate before the next QW layer would be grown, which does not match our structure as discussed earlier. Furthermore, the separate values of x_{ss} and L for each interface may not be a good model. It is difficult to interpret the meaning of two different x_{ss} values, for example, since this should correspond to the Sb flux. For structures in which more elements are varying across the QW/spacer interface, such as for an InAs/GaSb SL structure, this model may be more valid since the segregating and steady-state species are entirely different at the two interfaces. Based on the comparison of results of the Muraki and sigmoidal fits for the material analyzed in this work discussed above, the Muraki model was determined to be more valid for this structure and was used for further analysis.

For further understanding of the observed Sb variations in Figs. 4(b) (Multimedia view) and 5, the Muraki–Wood model was fit to each period individually, and the values for R, x_{ss}, and x_0 were extracted. Periods 704 and 705 were not fit due to the effect of the growth interrupt, which nearly eliminated the InAsSb layer in period 704 and substantially lowered the Sb in the InAs layer before period 705. The results are shown in Fig. 6. As seen from the individual fits, each parameter varies from period to period. What is most telling, however, is whether or not a trend exists across the analyzed region. For the segregation coefficient, R, the value is consistent within the given error bars. This even holds true for the periods nearest the growth interrupt, which have no indication of being affected by the interrupt. The same trend is seen for x_0, where the background Sb concentration stays consistent. This trend was also observed in the 1D composition profile of the full structure, as seen in Fig. 4(b) (Multimedia view), corroborating the data as observed in a separate analysis.

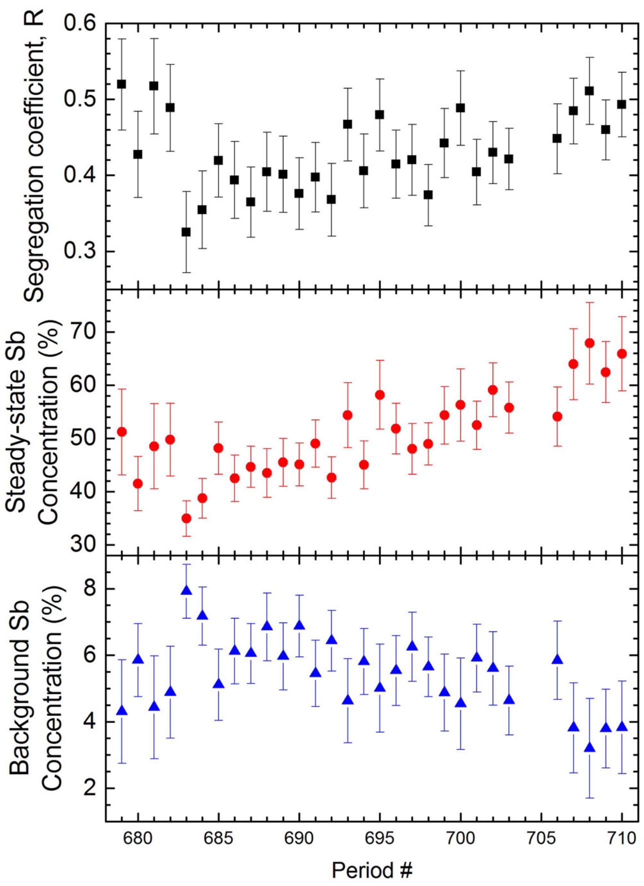

FIG. 6. The resulting R, x_{ss}, and x_0 values from the Muraki–Wood fit of each period analyzed. Period numbers run from low to high moving away from the substrate. Note: Periods 704 and 705 were omitted from the analysis due to the effect of the growth interrupt.

For the x_{ss} values, however, there is an observed shift from the periods grown first to those grown last as also seen in Fig. 4(b) (Multimedia view). It has previously been seen in the literature that, over a range of 80 periods, later periods in SL structures will have a higher Sb peak concentration than periods that were grown earlier in the structure.[3] Such a difference could be attributed to an increasing buildup of Sb background pressure in the growth

chamber during the thick absorber growth, leading to more Sb available for incorporation as the growth progresses. This indicates that there is an existing population of Sb adatoms migrating with the growth plane, increasing in population during InAsSb growth, and failing to incorporate during InAs layer growth due to conditions favoring preservation of the adatom state. Given the error bars in the determination of x_{ss} for each period, only the last four periods, which were after the growth interrupt, are clearly outside of the range of the earlier periods. Since this analysis only includes 31 of 734 periods, the apparent trend of increasing Sb may not be representative of the growth variations throughout the entire SL growth. To investigate the larger trends, future work will examine comparably sized regions of the SL taken from the beginning and middle of the stack.

IV. CONCLUSIONS

The development of high performance Ga-free T2SLs for MWIR photodetectors relies on a complete understanding of the band structure of the material. This band structure is a function of interface quality, including any non-abruptness caused by the spread of Sb atoms into layers intended to be Sb-free or slow incorporation in Sb-containing layers. In this work, we use APT to harvest 3D compositional data in an MWIR *nBn* T2SL photodetector consisting of 734 periods of alternating InAs and InAsSb, of which 31 total periods were analyzed. The resulting analysis shows an asymmetric Sb profile, a non-negligible concentration of Sb in the InAs layers, and a below-target Sb concentration in the InAsSb layers. These profiles demonstrate corroboration of a non-binary Sb profile as observed on similar systems using complementary techniques. The observed Sb concentration profile can be introduced into bandstructure models enabling a more accurate calculation of material parameters such as bandgap, conduction/valence band offsets, and carrier effective masses. Further study would examine the effect of growth conditions on the Sb incorporation by comparing the concentration profiles within and perpendicular to the growth plane using APT, as well as examining different regions of the SL stack to identify possible trends in the Sb concentration as the growth progresses.

ACKNOWLEDGMENTS

N.A.K. acknowledges support from the Karles Fellowship program at NRL. M.B.K. acknowledges support from the National Research Council Research Associateship Program. Additional support was provided by the Office of Naval Research (ONR).

DATA AVAILABILITY

The data that support the findings of this study are available from the corresponding author upon reasonable request.

REFERENCES

[1] B. V. Olson, E. A. Shaner, J. K. Kim, J. F. Klem, S. D. Hawkins, L. M. Murray, J. P. Prineas, M. E. Flatté, and T. F. Boggess, Appl. Phys. Lett. **101**, 092109 (2012).

[2] D. Z. Ting, S. B. Rafol, S. A. Keo, J. Nguyen, A. Khoshakhlagh, A. Soibel, L. Höglund, A. M. Fisher, E. M. Luong, J. M. Mumolo, J. K. Liu, and S. D. Gunapala, IEEE Photon. J. **10**, 6804106 (2018).

[3] M. R. Wood, K. Kanedy, F. Lopez, M. Weimer, J. F. Klem, S. D. Hawkins, E. A. Shaner, and J. K. Kim, J. Cryst. Growth **425**, 110 (2015).

[4] J. Lu, E. Luna, T. Aoki, E. H. Steenbergen, Y.-H. Zhang, and D. J. Smith, J. Appl. Phys. **119**, 095702 (2016).

[5] H. Kim, Y. Meng, J. F. Klem, S. D. Hawkins, J. K. Kim, and J.-M. Zuo, J. Appl. Phys. **123**, 161521 (2018).

[6] J. Steinshnider, M. Weimer, R. Kaspi, and G. Turner, Phys. Rev. Lett. **85**, 2953 (2000).

[7] H. J. Haugan, K. Mahalingam, F. Szmulowicz, and G. J. Brown, J. Cryst. Growth **436**, 134 (2016).

[8] K. Kanedy, F. Lopez, M. R. Wood, C. F. Gmachl, M. Weimer, J. F. Klem, S. D. Hawkins, E. A. Shaner, and J. K. Kim, Appl. Phys. Lett. **112**, 042105 (2018).

[9] M. W. Wang, D. A. Collins, T. C. McGill, S. T. J. Watson, R. W. Grant, and R. M. Feenstra, Appl. Phys. Lett. **66**, 2981 (1995).

[10] S. B. Rejeb, M. Debbichi, M. Said, A. Gassenq, E. Tournié, and P. Christol, J. Phys. D: Appl. Phys. **43**, 325102 (2010).

[11] K. Shiralagi, J. Shen, and R. Tsui, J. Electron. Mater. **26**, 1417 (1997).

[12] F. Szmulowicz, H. Haugan, and G. J. Brown, Phys. Rev. B **69**, 155321 (2004).

[13] X. Lü, L. Schrottke, E. Luna, and H. T. Grahn, Appl. Phys. Lett. **104**, 232106 (2014).

[14] M. Müller, A. Cerezo, G. D. W. Smith, L. Chang, and S. S. A. Gerstl, Appl. Phys. Lett. **92**, 233115 (2008).

[15] F. Tang, M. P. Moody, T. L. Martin, P. A. J. Bagot, M. J. Kappers, and R. A. Oliver, Microsc. Microanal. **21**, 544 (2015).

[16] A. Maryński, G. Sek, A. Musiał, J. Andrzejewski, J. Misiewicz, C. Gilfert, J. P. Reithmaier, A. Capua, O. Karni, D. Gready, G. Eisenstein, G. Atiya, W. D. Kaplan, and S. Kölling, J. Appl. Phys. **114**, 094306 (2013).

[17] B. P. Gorman, A. G. Norman, D. Lawrence, T. Prosa, H. Guthrey, and M. Al-Jassim, in *Proceedings of 37th IEEE PVSC* (IEEE, Seattle, WA, 2011).

[18] D. Z. Ting, A. Soibel, A. Khoshakhlagh, S. B. Rafol, S. A. Keo, L. Höglund, A. M. Fisher, E. M. Luong, and S. D. Gunapala, Appl. Phys. Lett. **113**, 021101 (2018).

[19] D. R. Rhiger, E. P. Smith, B. P. Kolasa, J. K. Kim, J. F. Klem, and S. D. Hawkins, J. Electron. Mater. **45**, 4646 (2016).

[20] D. Lubyshev, J. M. Fastenau, X. Gu, A. W. K. Liu, J. Prineas, E. J. Koerperick, J. T. Olesberg, E. M. Jackson, J. A. Nolde, C. Yi, and E. H. Aifer, Proc. SPIE **7660**, 76601J (2010).

[21] D. Lubyshev, Y. Qiu, J. M. Fastenau, A. W. K. Liu, E. J. Koerperick, J. T. Olesberg, and D. Norton, Jr., Proc. SPIE **8268**, 82681A (2012).

[22] J. M. Fastenau, D. Lubyshev, Y. Qiu, A. W. K. Liu, E. J. Koerperick, J. T. Olesberg, and D. Norton, Jr., Infrared Phys. Technol. **59**, 158 (2013).

[23] K. Thompson, D. Lawrence, D. J. Larson, J. D. Olson, T. F. Kelly, and B. Gorman, Ultramicroscopy **107**, 131 (2007).

[24] D. J. Larson, T. J. Prosa, R. M. Ulfig, B. P. Geiser, and T. F. Kelly, *Local Electrode Atom Probe Tomography: A User's Guide* (Springer, New York, 2013), Chap. 6, pp. 163–199.

[25] E. M. Anderson and J. M. Millunchick, Surf. Sci. **667**, 45 (2018).

[26] K. Muraki, S. Fukatsu, Y. Shiraki, and R. Ito, Appl. Phys. Lett. **61**, 557 (1992).

[27] M. DeJarld, L. Yan, M. Luengo-Kovac, V. Sih, and J. Millunchick, J. Appl. Phys. **121**, 034301 (2017).

[28] A. M. Beltrán, E. A. Marquis, A. G. Taboada, J. M. Ripalda, J. M. García, and S. I. Molina, Ultramicroscopy **111**, 1073 (2011).

[29] B. Paulus, P. Fulde, and H. Stoll, Phys. Rev. B **54**, 2556 (1996).

[30] D. Lackner, O. J. Pitts, S. Najmi, P. Sandhu, K. L. Kavanagh, A. Yang, M. Steger, M. L. W. Thewalt, Y. Wang, D. W. McComb, C. R. Bolognesi, and S. P. Watkins, J. Cryst. Growth **311**, 3563 (2009).

[31] E. Luna, F. Ishikawa, P. D. Batista, and A. Trampert, Appl. Phys. Lett. **92**, 141913 (2008).

[32] E. Luna, Á. Guzmán, and A. Trampert, Phys. Rev. Lett. **109**, 126101 (2012).